EBioMedicine 41 (2019) 175–184

Contents lists available at ScienceDirect

EBioMedicine

journal homepage: www.ebiomedicine.com

EBioMedicine
Published by THE LANCET

Serial patient-derived orthotopic xenografting of adenoid cystic carcinomas recapitulates stable expression of phenotypic alterations and innervation

Ashley Cornett [a,b], Harleen K. Athwal [a,b,1], Emily Hill [a,b,1], George Murphy III [a,b], Kenji Yeoh [a,b], Christopher A. Moskaluk [c], Robert L. Witt [d], Nisha J. D'Silva [e,f,1], Seema Agarwal [g,1], Isabelle M.A. Lombaert [a,b,*]

[a] University of Michigan, Biointerfaces Institute, Ann Arbor, MI, United States
[b] University of Michigan, School of Dentistry, Department of Biologic and Materials Sciences, Ann Arbor, MI, United States
[c] University of Virginia, School of Medicine, Department of Pathology, Charlottesville, VA, United States
[d] Thomas Jefferson University, Department of Otolaryngology-Head and Neck Surgery, Philadelphia, PA, United States
[e] University of Michigan, School of Dentistry, Department of Periodontics and Oral Medicine, Ann Arbor, MI, United States
[f] University of Michigan, Medical School, Department of Pathology, Ann Arbor, MI, United States
[g] Georgetown University Medical Center, Department of Pathology, Center for Cell Reprogramming, Washington, DC, United States

ARTICLE INFO

Article history:
Received 9 January 2019
Received in revised form 1 February 2019
Accepted 6 February 2019
Available online 11 February 2019

Keywords:
Adenoid cystic carcinoma
Salivary gland
Orthotopic PDX model
Fidelity
Neural invasion
Drug treatment

ABSTRACT

Background: Patient-derived xenograft (PDX) models have significantly enhanced cancer research, and often serve as a robust model. However, enhanced growth rate and altered pathological phenotype with serial passages have repeatedly been shown in adenoid cystic carcinoma (ACC) PDX tumors, which is a major concern.
Methods: We evaluated the fidelity of ACCs in their natural habitat by performing ACC orthotopic xenotransplantation (PDOX) in salivary glands.
Findings: Our PDOX model enabled solid tumors to integrate within the local epithelial, stromal and neuronal environment. Over serial passages, PDOX tumors maintained their stereotypic *MYB-NFIB* translocation, and FGFR2 and ATM point mutations. Tumor growth rate and histopathology were retained, including ACCs hallmark presentations of cribriform, tubular, solid areas and innervation. We also demonstrate that the PDOX model retains its capacity as a tool for drug testing.
Interpretation: Unlike the precedent PDX model, our data shows that the PDOX is a superior model for future cancer biology and therapy research.
Fund: This work was supported by the National Institutes of Health (NIH)/National Institute of Dental and Craniofacial Research (NIDCR) grants DE022557, DE027034, and DE027551.

1. Introduction

New strategies are constantly being developed to better design therapies for combatting cancer. It has been well addressed that immortalized cancer cell lines or 2D growth of primary human tumor-derived cells provide some insights into the disease, but lack the 3D complexity of the clinical situation [1]. Instead, subcutaneous implantation of patient-derived tumor specimens in immune-deficient mice, known as the PDX model, opened up a variety of opportunities to model cancer [1]. By better reflecting the 3D heterogeneity within the tumor, the PDX provided an answer to the urgent need for translatable preclinical modeling and therapeutic testing. For example, multiple successes were obtained in unraveling tumor resistance against current therapies and new drug development [1–3]. However, PDX models come with obstacles. Endogenous primary tumor-environment interactions are not sustained with subcutaneous implantations, and tumor-specific tropism of distant metastasis is mostly not recapitulated [4]. Moreover, multiple reports recently disputed the assumption that PDX tumors faithfully maintain features of the primary tumor [1,5,6]. Distinct selection pressures result in the disappearance of original genomic and morphological characteristics, thus affecting outputs of targeted therapies. Therefore, the need for more stable models to meet the demands of precision medicine is high.

One type of tumor affected by the PDX limitations and drift selection is the adenoid cystic carcinoma (ACC) [7]. ACC is a rare relentless

* Corresponding author at: Biointerfaces Institute-NCRC, 2800 Plymouth Rd, Ann Arbor, MI 48109, United States.
E-mail address: lombaert@umich.edu (I.M.A. Lombaert).
[1] Contributed equally

https://doi.org/10.1016/j.ebiom.2019.02.011

Research in context

Evidence before this study

It has been clear that patient-derived xenograft (PDX) models significantly enhanced cancer research, and serve as a robust model. However, for head-and-neck adenoid cystic carcinomas (ACCs) PDX tissues, enhanced growth rate and altered phenotypes with serial passages has repeatedly been observed. Thus, the PDX model drastically limits correct output for research and preclinical screening purposes.

Added value to this study

To address these major concerns of the ACC PDX model, we developed a new PDX-derived orthotopic xenotransplantation (PDOX) model of ACCs in salivary submandibular glands. Over serial passages, we compared the PDOX tumors with the PDX model and the original human tumor, and found that genomic, molecular and phenotypic characteristics were maintained. Moreover, our PDOX model showed stable tumor growth and increased innervation; thus, demonstrating superior stability and fidelity of ACCs than in the PDX model. We also demonstrate the PDOX model is receptive to drug treatments.

Implications of all the available evidence

To our knowledge, this is the first serial creation and in depth comparison of the ACC models on the genetic, histo-pathological and *in vivo* drug testing level. We propose that the ACC PDOX model is better used as an *in vivo* tool for future cancer biology and therapy research, as it better reflects the clinical situation.

neoplasm arising in secretory glands, most commonly in salivary glands, mammary glands, lacrimal glands and smaller glands in the head and neck region. A patient's long-term 15-year survival rate is ~40% due to progressive relapses [8]. Characterized by an initial slow growth and perineural invasion, ACCs late insidious local spread and distant metastasis to the lung are the hallmark of the disease [9]. The t [6,9] (q22-23; p23-24) is a recurrent translocation in ACCs [10]. It consistently results in a fusion protein of the transcription factor *MYB*. In 57–86% of the cases *MYB* fuses with *NFIB*, which results in overexpressed MYB protein as the inhibitory miRNA-binding 3′UTR site is removed [8,11]. A major drawback in the development of new treatment plans for ACCs has been the difficulty in obtaining appropriate cell lines and animal models. ACCs are rare, and the field suffered from ACC cell lines that were proven to be contaminated or genetically different from the original tumor [12]. In 2011, Dr. Moskaluk's group [13] established the ACC PDX model, and recently, new primary PDX-derived ACC cells [14,15] were created and extensively validated over multiple passages to maintain genomic stability [14]. In contrast, ACC fidelity emerged to be less maintained in the PDX model than originally assumed. Tubular or cribriform ACC PDX tissue shifts towards more aggressive solid tumors, as early as the first passage [7]. ACC PDX tumors were shown to transform into neoplasms with increased mitoses and decreased contribution of stroma and inflammatory cells.

To circumvent the limitations of the ACC PDX model, we aimed to create a submandibular gland (SMG) implantation model. The patient-derived orthotopic xenotransplantation (PDOX) mouse model was first described 2 decades ago [16], but are often underutilized due to technical procedures related to intra-organ surgery. Here, tumor growth rate of ACCs along with genomic, molecular and pathological stability using our PDOX model was compared to the conventional PDX over serial passages. To date, this is the first extensive study evaluating the creation and advantages of a SMG PDOX model. Overall, our PDOX method provides an optimal glandular microenvironment for ACC development, and ensures maintenance of clinically relevant ACC characteristics compared to the current PDX model.

2. Materials and methods

2.1. PDX tumor sample used for PDOX and control human salivary glands

The ACCX11 human biopsy and ACC11 PDX tissue (P8) was received from Dr. C. Moskaluk (Virginia). The human ACC specimen, coded ACCX11 [13], was isolated from a sinonasal cavity site from a female patient, aged 55, as part of a primary tumor and evaluated as grade 3 (>30% solid [17]). Previous histological examination of the ACC11 PDX (P1) showed characteristic histology with the donor tissue [13].

Human salivary glands were received from Dr. Witt (Delaware) after proper consent, and received at the University of Michigan.

2.2. Establishment of PDOX tissue

All animal experiments were approved by the Animal Care and Use Committee at the University of Michigan. Adult 6–8 week old NOD Cg-*Prkdc*^{scid} *Il2rg*^{tm1Wjl}/Szj mice were purchased from Jackson Laboratory and housed in Specific Pathogen Free (SPF)/BSL2 rooms located in the AAALAC-accredited University of Michigan vivarium.

Tumor samples were collected and dissociated with a tumor dissociation kit according to the manufacturer's description (Miltenyi, 130-095-929). After dissociation, the number of cells was quantified and a fixed number of cells were separated for implantation. Prior to implantation, mice were anesthetized with isoflurane and ketamine/xylazine, as previously described [18]. The neck area was surgically opened to expose the submandibular glands and a 5uL cell suspension containing ACC cells was injected.

Mouse weight and tumor growth were monitored on a weekly basis. At certain time-points after cell injections or at 1–2 cm^3 of tumor size, mice were euthanized by carbon dioxide and cervical dislocation. Tumor and lung tissue were photographed, and divided for RNA lysis and/or fixation after gross indexing.

2.3. Histology and immunofluorescent staining

Formalin or paraformaldehyde fixed tissue was processed for paraffin sectioning, and stained with a routine hematoxylin-eosin stain or treated for immunohistochemistry. Immunofluorescent labeling of cryosections or paraffin-embedded sections was performed, as previously described [19]. The following antibodies were used: Ku80 (Cell Signaling Technology, 21805), KRT18 (Abcam, ab32118), ACTA2 (Sigma, A2547), TUBB3 (RnD Systems, mab1195), E-cadherin (Cell Signaling Technology, 3195S or BD Biosciences, 560062), Vimentin (Cell Signaling Technology, 5741S or Abcam, ab45939), PECAM (BD Biosciences, 550274 or SCBT, sc-53411), HNA (EMD Millipore, MAB1281), MYB (EMD Millipore, 05-175), CD68 (Abcam, ab5344), Ki67 (BD Biosciences, 550609), and COXIV (Cell Signaling, 4850). Fluorescently labeled secondary antibodies were used for protein visualization under a Leica confocal microscope. Nuclei were stained with DAPI (Fisher, D1306).

2.4. In situ hybridization (FISH)

In situ hybridization was performed with specific MYB/NFIB translocation probes (Abnova, FT0027) according to the manufacturer's instructions. Briefly, cryosections were hybridized with the fluorescently labeled target probes. Nuclei were counterstained with DAPI.

2.5. Gene expression analysis

Real time PCR was performed as previously described [19]. cDNA was generated from DNAse-free RNA, amplified and gene expression was normalized to human-specific house-keeping gene, *GAPDH*, and human control submandibular gland. Experiments were run in technical triplicates at a minimum of three biological samples, unless stated otherwise in the legends. All primers were designed to exclusively detect human gene expression and were found negative in generating amplicons from mouse submandibular gland tissue. Only as indicated in the legends of Figs. 3–4 and Supplementary Fig. 3, mouse-specific primers were used that did not generate amplicons on human tissue material. Graphs depict Mean ± SEM, representing 3 technical replicates (for $N = 1$ tissue samples) or biological replicates (for $N \geq 3$ tissue samples).

2.6. Quantification of tissue morphology

Hematoxylin-eosin slides of the ACCX11 human biopsy, PDX (P1, 3, and 8), PDOX($n + 1$), and PDX-S tissue were evaluated by pathologist NJD, and a percentage of the solid, cribriform and tubular form was defined. Data was plotted as a Mean ± SEM.

2.7. Drug sensitivity test

Tumor dimensions (mm) were converted to volume (mm^3) using the formula previously used on ACC11 PDX tissue: tumor volume (TV) = (width^2) × length × 0.52 [14]. Regorafenib was formulated for daily oral gavage injection with a final dose of [25 mg/kg], as directed by the manufacturer (SelleckChem, BAY 73-4506). Body weight and tumor measurements (digital caliper) were collected twice weekly. Each biweekly tumor volume, TV Day(n), measurement was normalized to its corresponding initial tumor volume, TV Day(0) pre-regorafineb, using the eq. TV norm = TV Day(n)/ TV Day(0). Statistical analysis on normalized final tumor size, control *vs* treatment, was performed using a two-tailed student *t*-test with Welch's correction.

2.8. Establishment of PDX-S tissue

ACC11 PDX (P8) tumor tissue was dissociated into single cells using the Miltenyi tumor dissociation kit (Miltenyi, 130-095-929) to generate subcutaneous PDX tumors (PDX-S). In each mouse, 3×10^5 cells were injected in Matrigel (Corning, Cat#356234), as previously described [20]. Control injections (matrigel without cells) were administered in the right flanks of the same mice. Body weight and tumor measurements were collected weekly. Tumor volume was calculated using the formula: TV = (width × 2) × length × 0.52 [14].

2.9. Sequencing

Using total RNA, cDNA was generated as described above. RT-PCR was performed with primers close to the mutation sites, as described previously [14]. Generated amplicons were analyzed *via* Sanger sequencing.

2.10. Relative tumor size

Increase of relative tumor size over time was calculated *via* the relative tumor volume equation, as described previously for the ACC PDX model [7]. Briefly, $R_0(t)$ and $R_p(t)$ were calculated over PDOX(n) passages and plotted in a log-transformed graph. $V_0(0)$ and $V_p(0)$ remained constant and reflected a standard measurement of control mice.

2.11. Body weight analysis over time

Weights of the mice were monitored on a weekly basis. The time of visible tumor initiation was defined as time zero, week zero or $W_{(0)}$. All weights before W0 (negative weeks) and after $W_{(0)}$ (positive weeks) were normalized to $W_{(0)}$. Weights of all mice across the four PDOX passages were averaged to create a mean ± SEM, and plotted into a graph. Subsequently, a trend line was created to reveal a constant increase in body weight over time.

2.12. Statistical analysis

Statistical parameters included $N \geq 3$. Data was analyzed to be statistically significant between two groups using one sample *t*-test or student's *t*-test, as indicated in the legends. Graphs show Mean ± SEM for each group. $P < .05$ was considered statistically significant. No statistical analysis could be performed between samples consisting of $N = 1$.

3. Results

3.1. The mouse submandibular gland is a suitable environment to harbor ACCs

To compare ACC tumor formation in a glandular environment with the subcutaneous ACC PDX model [13], we injected 0.7×10^6 single ACC cells into the salivary submandibular gland. A PDX passage 8 (P8) of a head-and-neck ACC, ACC11, was provided by Dr. Moskaluk [13] and used as initial tumor material. The PDX tissue was dissociated into single cells prior to transplantation (Fig. 1A). The contralateral gland was used as negative control and received a saline injection. ACC11-injected glands at 3 month post-injection showed no differences with the contralateral glands (Fig. 1B, Suppl. Fig. 1A). Gland weight and histology, including salivary acini and ducts, were found comparable (Suppl. Fig. 1B–C). At 4 months post-injection, ACC11 PDOX [1] tumors became visibly apparent (Fig. 1B, Suppl. Fig. 1A). By month 5, tumor size reached 1–2 cm^3 and increased the gland weight by 800% relative to control gland (Fig. 1B, Suppl. Fig. A, C).

To investigate the morphology of the tumor within the mouse SMG environment, we performed routine histology. ACC11 PDX (P1) tissue was previously classified as high grade 3 with >30–50% solid form depending on the applied grading system [17], and found to resemble the donor tumor [13] (Fig. 1C, Suppl. Fig. 1D). However, ACC11 PDX tissue became mixed solid/cribriform over multiple passages (Fig. 1C, Suppl. Fig. 1D–E). Stellate interstitial cells (Fig. 1C, arrow) and extravasated erythrocytes were present in the PDX tissue (Suppl. Fig. 1E). By 4 and 5 months, the PDOX [1] tumor became apparent and showed characteristic solid, cribriform, and tubular morphology with neoplastic cells invading adjacent mouse salivary gland (Fig. 1C, Suppl. Fig. 1D–E), skeletal muscle and approximating nerves (Fig. 1D). Consistent with features of human ACC, the neoplastic cells in the PDOX exhibited ovoid and spindle-shaped nuclei with minimal cytoplasm, characteristics for de-differentiation (Fig. 1D, yellow arrow). Malignant transformation from low-grade to high-grade, or de-differentiation, has been associated with ACCs and corresponds to an aggressive clinical course [21]. Mitoses, typically identified in ACC with solid features, were also observed (Fig. 1D, dashed yellow arrows). To confirm the human origin of the PDOX tumor, we performed human specific Ku80 staining. As predicted, malignant cells were $Ku80^+$ while surrounding mouse tissue showed no expression (Fig. 1E, Suppl. Fig. 1F).

Next, we investigated the genomic and molecular profile of the ACC11 PDOX tumor. The donor patient's tumor and ACC11 PDX (P8) tissue harbored the *MYB-NFIB* translocation [13] (Fig. 1G). Through fluorescent *in situ* hybridization (FISH) and qPCR analysis (Fig. 1F–G), we confirmed that the *MYB-NFIB* gene translocation (Fig. 1F) as well as *MYB-NFIB* fusion mRNA (Fig. 1G) is present in PDOX [1] tissue. As

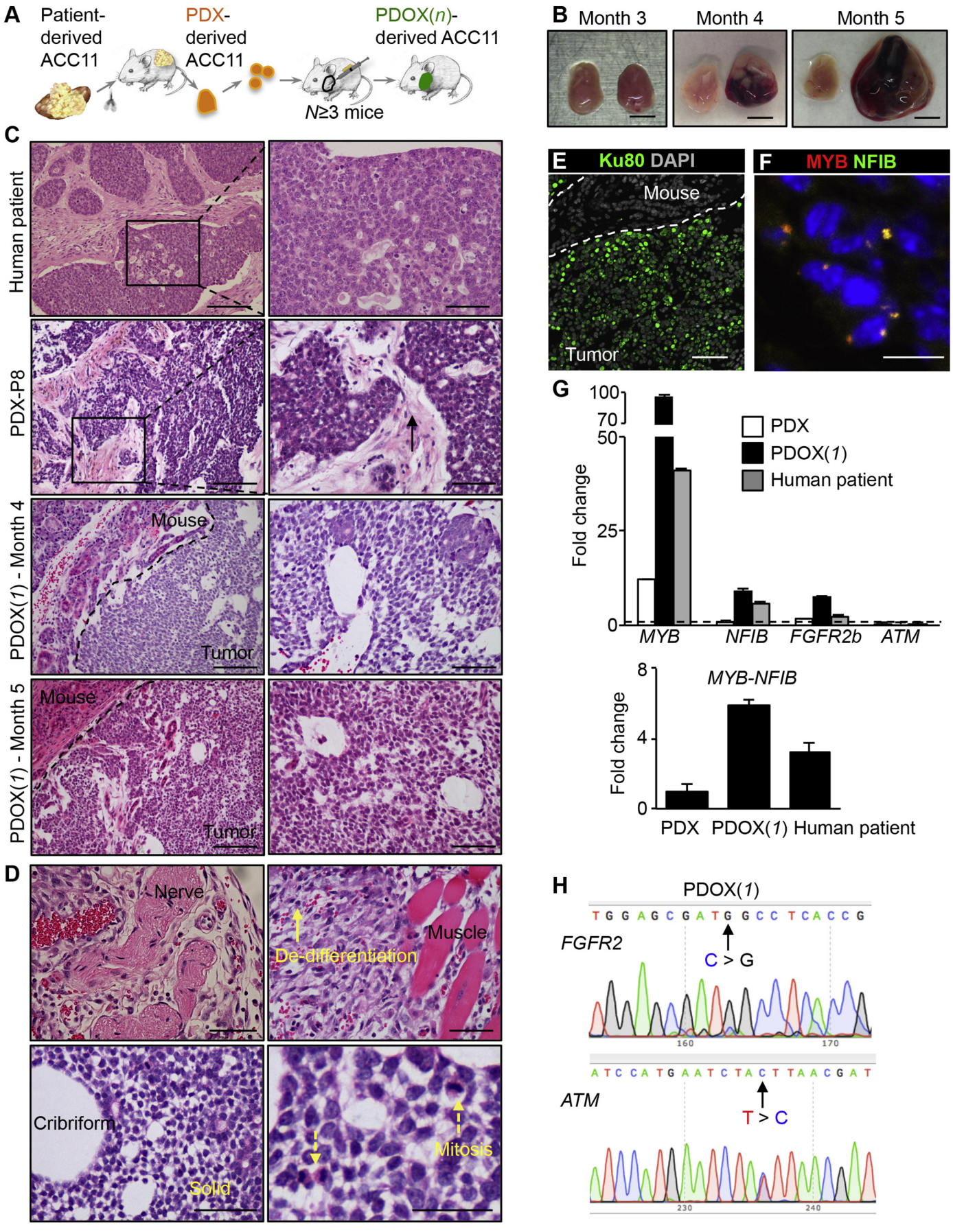
A
Patient-derived ACC11
PDX-derived ACC11
PDOX(n)-derived ACC11
N≥3 mice
B
Month 3
Month 4
Month 5
C
Human patient
PDX-P8
PDOX(1) - Month 4
PDOX(1) - Month 5
Mouse
Tumor
D
Nerve
Muscle
De-differentiation
Cribriform
Solid
Mitosis
E
Ku80 DAPI
Mouse
Tumor
F
MYB NFIB
G
Fold change
PDX
PDOX(1)
Human patient
MYB
NFIB
FGFR2b
ATM
MYB-NFIB
PDX PDOX(1) Human patient
H
PDOX(1)
FGFR2
C > G
ATM
T > C

expected from the gene fusion, PDX and PDOX [1] tumors showed increased *MYB* gene expression levels compared to normal human SMG (dotted line) (Fig. 1G). Interestingly, within the first passage of switching to the PDOX model, *NFIB*, *MYB* and *MYB-NFIB* expression levels were restored to more clinically relevant levels, resembling the human patients biopsy. No *MYB-NFIB* amplicon, specifically designed over the ACC11 *MYB-NFIB* breaking point, was generated in normal human SMG (SMGs). With the additional FGFR2 S252 W and ATM F858 L point mutations present in the ACC11 PDX [14], we confirmed the presence of the C > G (*FGFR2*) and T > C (*ATM*) conversion in ACC11 PDOX [1] (Fig. 1H). The gain-of-function S252 W mutation [22] automatically leads to increased *FGFR2b* expression levels (Fig. 1G). Since the effect of missense F858 L on ATM protein is unknown and the mutation lies outside the functional protein domain [23], no increased *ATM* was observed in the PDX or PDOX [1] tissue (Fig. 1G).

These findings indicate that SMGs offer a suitable environment for ACC expansion using single cell suspension fluid transplantation. Tumor growth initiated between 3 and 4 months and maintained the genomic and morphological phenotype of the original PDX (P8) donor tissue, and a single PDOX passage rescued molecular similarities consistent with the human specimen that were lost during passaging using the PDX method.

3.2. Serially transplanted PDOX tumors maintain distinctive ACC traits

After initiating the PDOX model, we evaluated the concordant nature of serial PDOX transplantations (Fig. 2A). An ACC11 tumor from transplant *n*, PDOX(*n*), was dissociated into single cells, and various cell numbers were injected into new acceptor mice to generate PDOX ($n + 1$) tissue (Fig. 2A–B). In each PDOX(*n*) cycle, we obtained a 100% success rate in obtaining tumors (Fig. 2C). Across 4 serial transplantations, tumor growth rate reaching $1cm^3$ remained constant between 3 and 4 months (Fig. 2D, arrow). We next calculated the 'relative tumor size increase' of the PDOX's from 1 to P4. This mathematical equation combines and normalizes tumor size information over multiple passages, allowing evaluation of tumor growth rate behavior over time periods exceeding the life span of the mouse. Interestingly, the calculated PDOX 'relative tumor size increase' over the lifetime of the serial transplants revealed constant growth (Fig. 2E), which is in striking contrast to the accelerated growth seen in the PDX model [7]. Also of interest is that the outwards growth of the PDOX tumors in the salivary glands did not affect the feeding capacity of the host, as indicated by the ceaseless increase in mice body weight over time (Suppl. Fig. 2A).

Histologic comparison of the PDOX(*n*) tumors to PDOX [1] showed no apparent differences in tumor morphology exhibiting tubular, cribriform and solid arrangement of tumor cells (Fig. 2F, Suppl. Fig. 2B, Suppl. Fig. 1E). All ACC11 PDOX(*n*) neoplasms exhibited $Ku80^+$ cells (Fig. 2G, Suppl. Fig. 2C). Moreover, *MYB-NFIB* as well as the *FGFR2* and *ATM* point mutations were found present across the PDOX(*n*) transplantations (Fig. 2H–I, Suppl. Fig. 2D). Increased mRNA levels of *MYB*, *NFIB* and *FGFR2b* were also preserved over PDOX(*n*) tumors (Fig. 2H).

Overall, these data reveal that the PDOX model maintains the distinctive genomic, morphological, and molecular features of ACCs over time.

The salivary gland PDOX model is sufficient to recapitulate the clinical neural, endothelial and stromal environment for ACCs.

After evaluating the genomic and molecular fidelity of PDOX tumors, we investigated the epithelial, stromal and neural components within the ACCs. We compared protein and gene expression of PDOX(*n*) with PDX (P8), normal mouse and human SMGs, and human patient ACCX11. PDOX(*n*) tumors shared epithelial cells (CDH1, ECADHERIN) dominant in myoepithelial cell marker smooth muscle actin (ACTA2) with ACCX11 (Fig. 3A–B (arrows), Suppl. Fig. 3A–B), which is characteristic for cribriform and tubular ACCs [24]. PDX tissue appeared heterogeneous, and consisted of areas with an epithelial only and strong interstitial epithelial-myoepithelial character. In both ACCX11, PDX, PDOX(*n*) tissue, stromal marker, vimentin (VIM), was highly expressed and surrounding the neoplastic epithelial and/or epithelial-myoepithelial cells. The latter cell type is known to express vimentin across various salivary gland neoplasms [24]. In contrast, myoepithelial cells surround ducts and acini in normal human/mouse SMGs, and vimentin is only expressed in stroma to engulf the main ducts. Typical ACC-related MYB protein expression and high cell division (Ki67 and CCND1) were found in ACCX11, PDX and PDOX(*n*) tumors (Fig. 3C, Suppl. Fig. 3C). Fold changes in gene expression confirmed protein expression by showing increased levels of *ACTA2* in ACCX11 and PDOX(*n*) tissue, compared to PDX (Fig. 3B). Basal epithelial and myoepithelial marker *KRT14* was also increased in ACCX11 and PDOX(*n*) tissue compared to PDX, but ductal marker *KRT19* remained rather similar. As expected, vimentin (*VIM*) and *CCND1* were upregulated in both PDX and PDOX(*n*) tissue.

Thus, proper epithelial/stromal contribution and high proliferative status are preserved in the PDOX(*n*) model, and showed more similarities with ACCX11 than PDX.

To evaluate the clinically relevant perineural character of ACCs, in particular ACCX11, we assessed the neuronal/endothelial component. Neuronal (TUBB3) and endothelial (PECAM) cells are dispersed within the stromal compartment, and surround epithelial cells in normal mouse/human SMGs (Suppl. Fig. 3D–E). Sporadically, nerves and dispersed blood vessels were found within the PDX tissue. In contrast, extensive innervation and presence of blood vessels were present in PDOX(*n*) tumors (Fig. 3D–E, arrows). Neuronal cells and/or nerve fibers [25] were predominantly observed within the solid epithelial compartment, as well as close to the luminal lining of cribriform areas (Fig. 3D). Related to the neural observation seen in ACCX11, increased gene expression levels of human-related neurotrophic factors (neurturin *NRTN*, nerve growth factor *NGF*, brain derived neurotrophic factor *BDNF*) were observed in PDOX(*n*) tumors compared to PDX tissue (Fig. 3F). Only mouse-specific *Pecam* could be detected in all PDX and PDOX(*n*) tumors while human-specific *PECAM* was solely observed in human SMG and ACCX11 (Fig. 3F, Suppl. Fig. 3F). Interestingly, both mouse-specific *Tubb3* and human-specific *TUBB3* were detectable in both PDX and PDOX(*n*) samples (Fig. 3F), indicating that both tumor-related and host-specific nerves contribute to the perineural effect observed in the *in vivo* generated tumors. Notwithstanding, PDOX tumors contained more gene expression levels of both *Tubb3* and *TUBB3* compared to PDX, confirming the histological observation. Overall, these observations reveal that the SMG PDOX model robustly mimics the clinical relevant environment, allowing for stable formation of ACCs over serial transplantations.

Fig. 1. The SMG is a suitable environment to harbor ACCs. (A) Cartoon depicting the creation of the PDOX mouse model. PDX tissue was created from a patient-derived ACC, termed ACCX11. This ACC11 PDX tissue was passaged 8 times using the PDX model, and PDX (P8) was dissociated into single cells prior to transplantation into the mouse salivary gland. Several months later, the first ($N = 1$) PDOX tumor was generated. (B) Bright field pictures of PDOX [1] at 3, 4 and 5 months post-cell injection. The contralateral gland served as control (left). Scale bar, 0.5 cm. (C) Comparison of the histology (hematoxylin-eosin, HE) between ACCX11 (human patient), ACC11 PDX (Passage 8, P8), and ACC11 PDOX [1] tissue at months 4 and 5. Right panels are high power images from the same sections of which a part is shown on the left. Scale bar, 500 μm (left panels) and 250 μm (right panels, arrow indicates stellate cells). (D) High power HE images of ACC11 PDOX [1] tumors outlining nerve and muscle integration, existence of cribriform/solid form, mitoses (dashed yellow arrows) and de-differentiation (yellow arrow). Scale bar, 500 μm (upper panels), 125 μm (lower left panel) and 75 μm (lower right panel). (E) Human-specific Ku80 staining and nuclei (DAPI) in PDOX [1] tissue. Scale bar, 50 μm. (F) Fluorescent *in situ* hybridization of PDOX [1] tumor outlining the *MYB-NFIB* gene translocation. Nuclei (DAPI). Scale bar, 12 μm. (G) qPCR analysis of ACC-related genes in ACCX11 ($N = 1$), ACC11 PDX P8 ($N = 1$) and PDOX [1] tumors ($N = 1$). Gene expression levels were normalized to human specific housekeeping gene *GAPDH* and normal human SMG (dotted line), except for *MYB-NFIB* as the translocation is not present in normal SMG. *MYB-NIFB* data was normalized to PDX tissue. Mean ± SEM. (H) Sequencing of *FGFR2* and *ATM* transcripts showing ACC11's unique point mutations F858L (C > G) and S252 W (T > C), respectively, in PDOX [1].

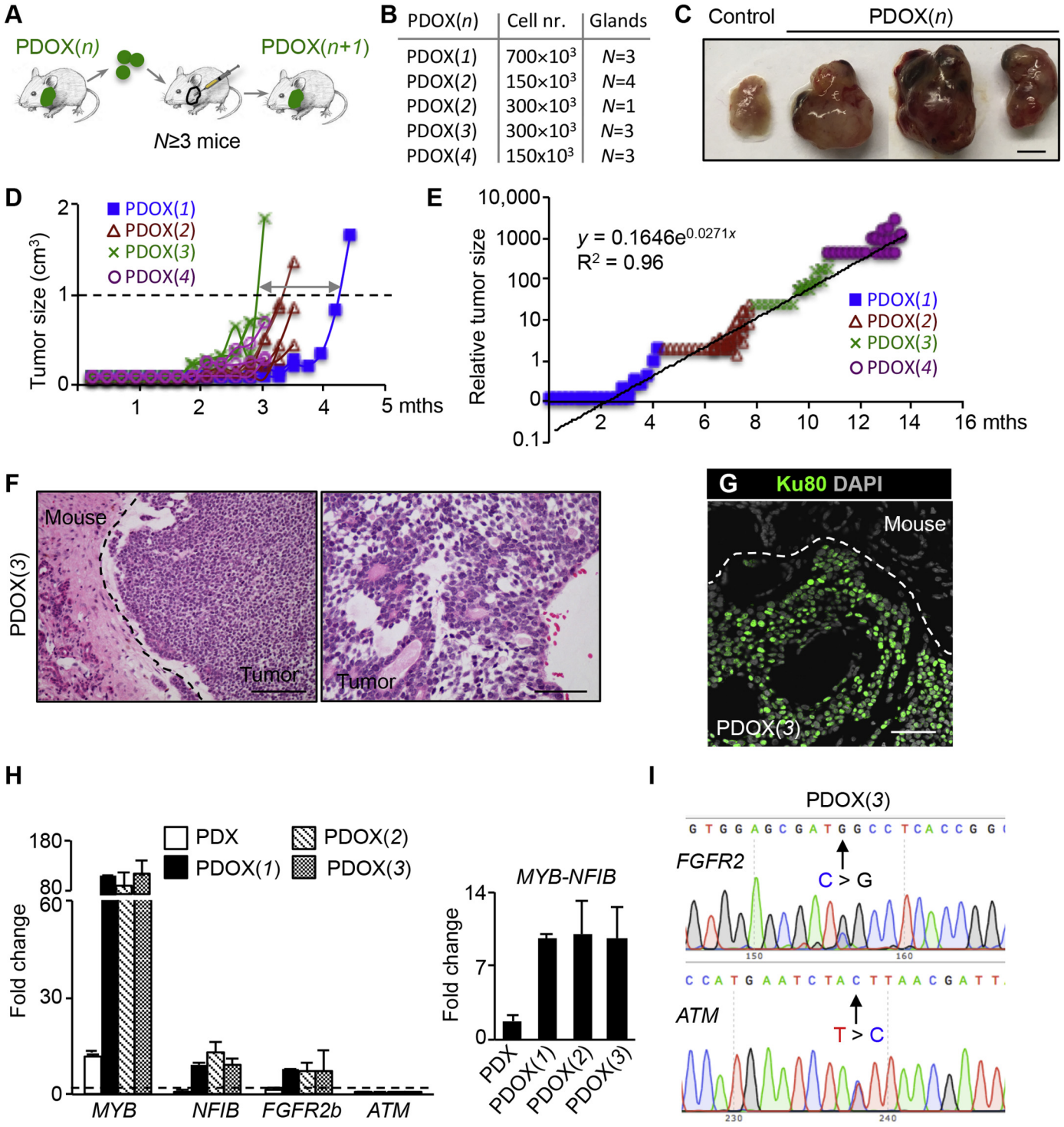

Fig. 2. Serially transplanted PDOX tumors maintain distinctive ACC traits. (A) Cartoon illustrating the PDOX($n+1$) serial transplantation model. (B) Number of transplanted cells into the various PDOX($n+1$) mice. (C) Representative examples of PDOX($n+1$) tumors compared to a contralateral control gland. Scale bar, 0.5 cm. (D) Graph outlining tumor growth size over time for each PDOX($n+1$) tumor. (E) Graph showing relative tumor growth increase over serial passages. (F) HE staining of PDOX [3] tumors. Scale bar, 500 μm (left) and 250 μm (right). (G) Ku80 and nuclear (DAPI) staining on PDOX [3] tumor tissue. Scale bar, 50 μm. (H) Fold changes in gene expression of ACC11 PDX and PDOX($n+1$) tumors. Data was normalized to *GAPDH* and normal human SMG (dotted line), except for *MYB-NFIB*. PDX ($N=1$), PDOX [1] ($N=1$), PDOX [2] ($N=3$), PDOX [3] ($N=3$). Mean ± SEM. One sample *t*-test. (I) Presence of point mutations in *FGFR2* and *ATM* in PDOX [3] tumor, as defined by sequencing.

3.3. Evaluation of drug sensitivity and metastasis in PDOX(n) model

To demonstrate the efficacy of the PDOX model for drug testing, we evaluated PDOX [4] tumors treated with buffered-saline or Regorafineb, which inhibits ACC11 PDX tumors [14]. As expected, Regorafineb significantly inhibited tumor growth size by 28 days of treatment (Fig. 4A), demonstrating the capabilities of the PDOX model for future drug testing.

With ACCs being known for their preferential metastasis to the lung, we explored the presence of ACC11 cells in the lung. Gross indexing of

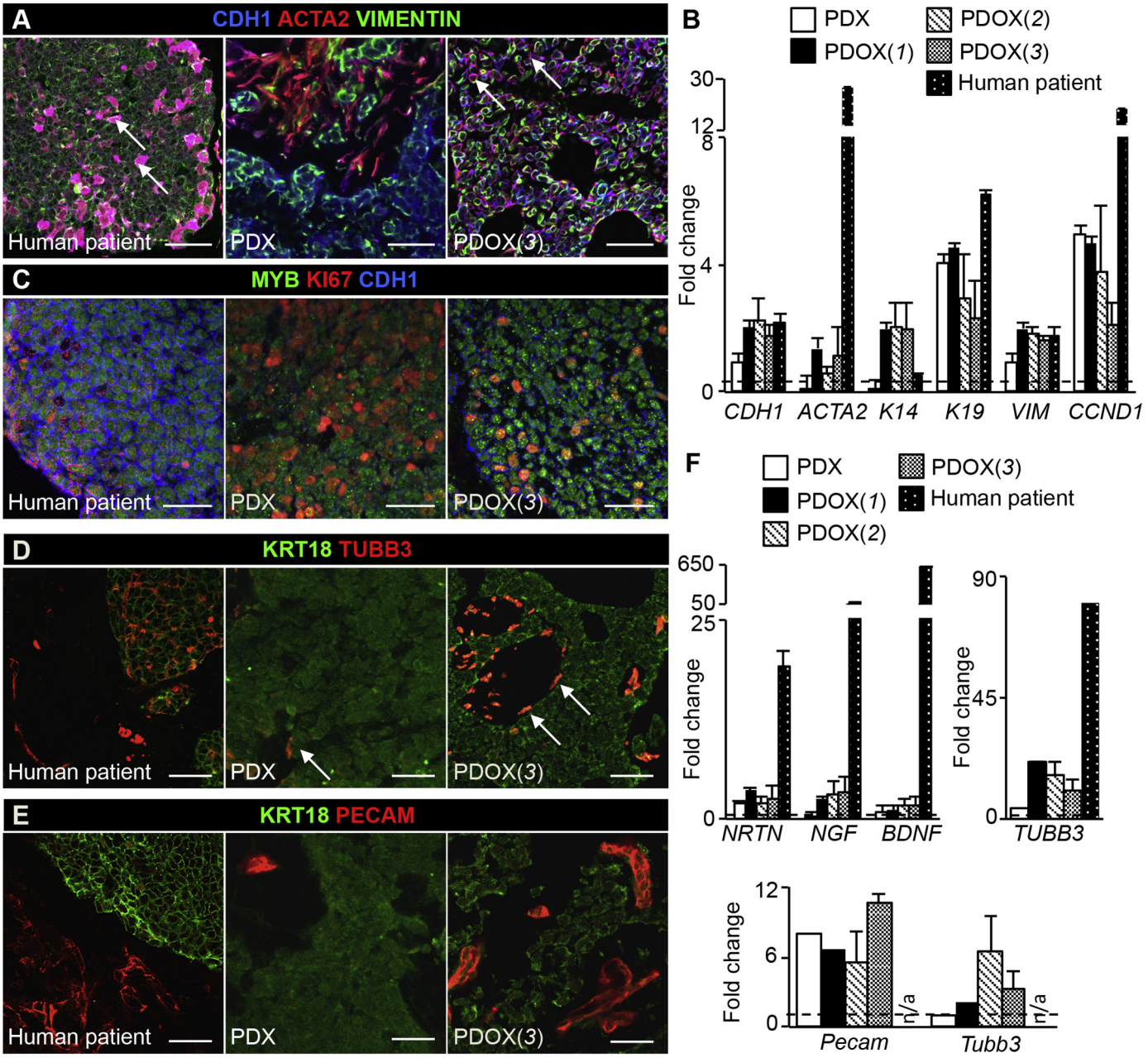

Fig. 3. The PDOX model is sufficient to recapitulate the clinical neural, endothelial and stromal environment for ACCs. (A, C, D, E) Protein staining for MYB, KI67, epithelial (ECADHERIN, CDH1 or KRT18), myoepithelial (ACTA2), stromal (VIMENTIN, VIM), neuronal (TUBB3), endothelial (PECAM) cells on ACCX11, PDX (P8) and PDOX [3] tumor. Scale bars, 50 μm. Arrows represent CDH1$^+$ cells expressing ACTA2 (A), or presence of innervation (D). (B, F) qPCR analysis of human-specific epithelial, neuronal, and stromal-related genes in PDX (P8), PDOX(*n*) tumors, and ACCX11. Data was normalized to *GAPDH* and normal human SMG, except for mouse-specific primers *Pecam* and *Tubb3*. This data was normalized to control mouse SMG and normalized to mouse *Gapdh*. ACCX11 ($N = 1$), PDX (P8) ($N = 1$), PDOX [1] ($N = 1$), PDOX [2] ($N = 3$), PDOX [3] ($N = 3$). Mean ± SEM. One sample *t*-test.

PDOX(*n*) lungs compared to normal lung did not show apparent neoplasms, except for small areas of unhealthy tissue (Fig. 4B, arrows). Through histology, we observed the presence of macrophage-like cells across all PDOX(*n*) lungs (Fig. 4C, arrows). By observing human-specific nuclear antigen (HNA) protein (Fig. 4D) or human-specific mitochondrial cytochrome *c* protein (COXIV) (Suppl. Fig. 4A) with mouse-specific CD68 protein, we found that PDOX(*n*) lungs contained more CD68$^+$ macrophages. The latter were not HNA$^+$/COXIV$^+$, and no other epithelial (CDH1) HNA$^+$/COXIV$^+$ cells were observed in the lung at 4 months. Possibly, this 4-month time frame post-injection may be too early to detect metastasis.

To demonstrate the validity of using single cells in the PDOX model, we further compared tumors generated subcutaneously from ACC11 PDX (P8) single cells (PDX-S) (Fig. 4E). PDX-S tumors showed a similar growth rate of 3–4 months (Fig. 4F–G). They appeared similar to PDX (P1–3) (solid 80–90%, tubular 0–5%, cribriform 0–10%) tumors (Fig. 4H), often in vicinity of necrotic areas. Phenotypically, PDX-S tissue showed similar results as PDX (P8) in epithelial (CDH1) cells expressing MYB, KI67, but devoid of ACTA2 (Fig. 4I). Interestingly, blood vessels were present and in certain areas a big ganglia were observed, however axon integration was absent. No lung metastasis was observed at 3–4 months (Fig. 4J). Molecularly, PDX-S tissue showed lower expression of *MYB-NFIB*, *ACTA2*, and *KRT14* relative to PDOX(*n*) and that were similar to PDX (Fig. 4K–L). Except for *NGF*, similar levels of *NRTN*, and *BDNF* could be observed in PDX-S compared to PDX (Fig. 4M). Levels of mouse-specific *Pecam* in PDX-S were similar to PDX and PDOX tissue, and no human *PECAM* was present (Suppl. Fig. 3F). While human *TUBB3* was similar to PDOX [1] and higher than PDX, mouse *Tubb3* was

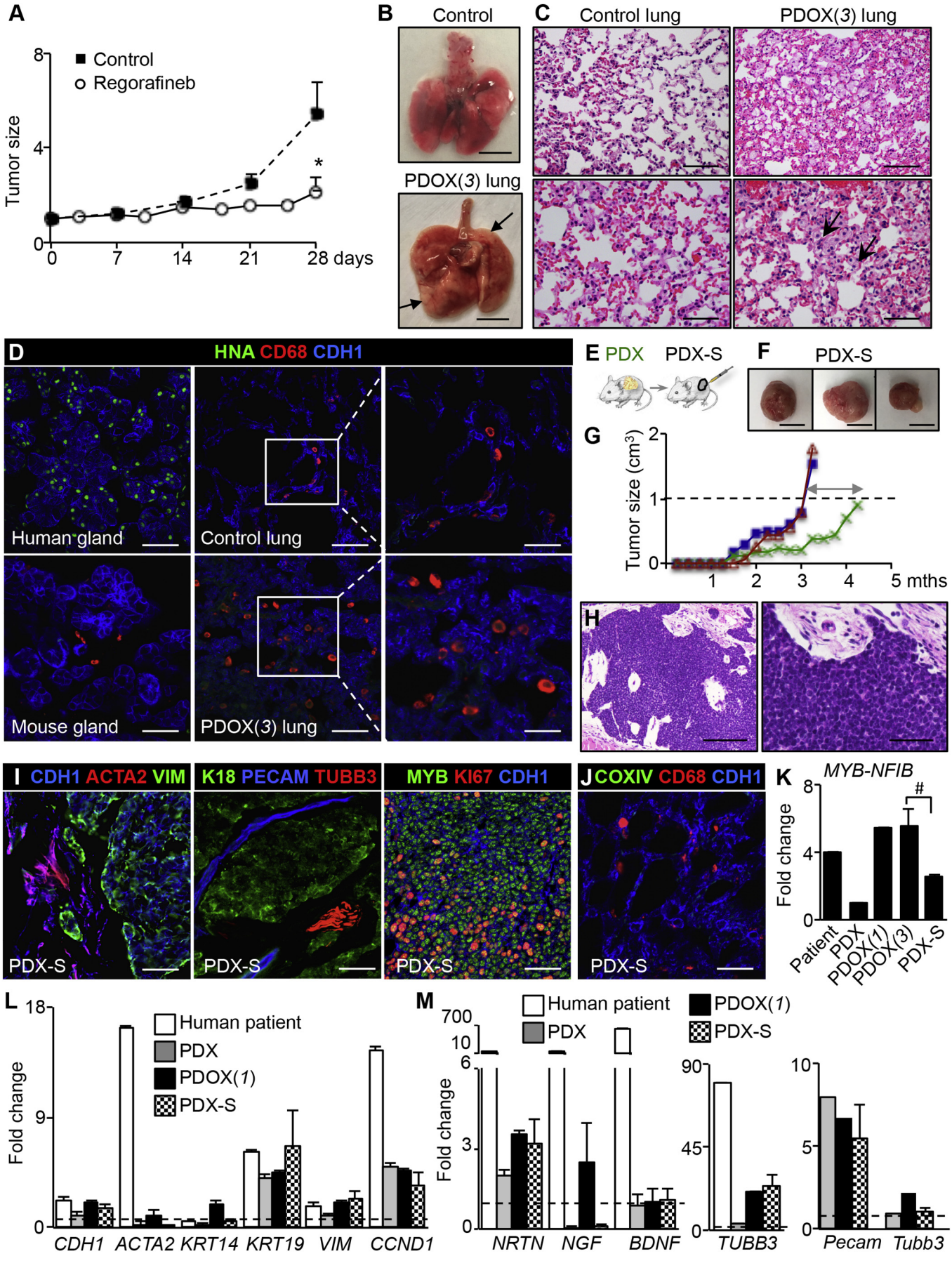
A
Control
Regorafineb
Tumor size
8
4
0
0
7
14
21
28 days
*
B
Control
PDOX(3) lung
C
Control lung
PDOX(3) lung
D
HNA CD68 CDH1
Human gland
Control lung
Mouse gland
PDOX(3) lung
E PDX
PDX-S
F
PDX-S
G
Tumor size (cm3)
2
1
0
1
2
3
4
5 mths
H
I CDH1 ACTA2 VIM
K18 PECAM TUBB3
MYB KI67 CDH1
J COXIV CD68 CDH1
PDX-S
K
MYB-NFIB
Fold change
8
4
0
#
Patient
PDX
PDOX(1)
PDOX(3)
PDX-S
L
Human patient
PDX
PDOX(1)
PDX-S
Fold change
18
9
0
CDH1
ACTA2
KRT14
KRT19
VIM
CCND1
M
Human patient
PDX
PDOX(1)
PDX-S
Fold change
700
10
6
3
0
NRTN
NGF
BDNF
90
45
0
TUBB3
10
5
0
Pecam
Tubb3

lower, indicating that the host-related innervation is lower in PDX-S compared to the PDOX model. This indicates that the PDX-S model better mimics the ACC environment then the PDX model, but does not phenocopy the ACC tumor cells as in the clinical setting.

Thus, our PDOX model shows superior environmental and ACC characteristics over the PDX and PDX-S model. Moreover, tumor fidelity is maintained over multiple passages, which is in striking contrast to the PDX set-up.

4. Discussion

For each cancer model it is utterly important to understand the unique opportunities it has to offer, as well as the limitations. Particular caution should be given towards genomic instability and pathological changes that distance the newly generated tumors from the original specimen. Here we evaluated tumor fidelity and environmental phenotype in our glandular PDOX against the current PDX model, as the latter had been suffering from clonal drifting and altered genomic composition [5]. Our PDOX model did not show drastic changes in tumor growth rate or overall infidelity. It also maintained profuse innervation, which often relates to the metastatic component of ACCs and poor prognosis [26,27], and was validated for drug testing.

PDOX models often harbor a powerful advantage over PDX as clinical features like metastasis can be more readily observed. Due to the subcutaneous tumor location, the vast majority of the PDX tumors retain local tumor expansion with circumscribed borders without apparent invasion. Instead, orthotopic transplantation of tumor-derived single cells or spheres better mimicked drug response, tumor growth pattern and clinically-relevant metastasis [4]. Surprisingly, PDOX models are still limited to mammary gland [28,29], lung [30], pancreas [31], brain [32], colon [16], stomach [33], ovaria [34] and cervix [35], even though the first PDOX was established in 1991 [16]. We now add salivary submandibular glands as a successful intra-organ model to generate tumors, such as ACCs. We propose that metastasis should be feasible as the increased innervation is preserved over our serial PDOX tissue. Unfortunately, no ACC11 metastasis was observed to the lung within the limited time frame before harvesting the primary tumor. While ACC11 PDX tissue takes 10 months to develop [13], ACC11 cells clearly expand quicker (3–4 months) in their original intra-organ environment. On rare occasion, undissociated ACC specimens, either transplanted subcutaneously or in the center of the tongue, were shown to metastasize to the lung 5 months after transplantation [36]. These ACCs had a pure solid pattern, known to harbor the worst prognosis for metastasis. It is currently unclear whether the patient from whom ACC11 PDX was derived had lung metastases. As such, ultimate validation of lung metastasis in our PDOX model will involve transplantation of ACCs known to have metastasized in the patient, and/or increase the experimental time frame before tissue harvesting. While our new PDOX model is superior over the current *in vivo* PDX set-up for pre-clinical studies, the speed by which the ACC PDOX tumors are formed and/or metastasize is too slow for clinical-related settings where real-time testable therapeutic outcomes are required, for example within 1–2 weeks. For those 'personalized medicine'-intended purposes, the creation of *ex vivo* 3D tumor spheroids in multi-well plates [37] can serve as a reliable method for rapid drug screening assays. Multiple salivary gland cancers, including ACCs, have sphere-forming potential and share common *ex vivo* phenotypes in that similar ($ALDH^{+}CD44^{high}$) epithelial tumor stem cell populations form the highest numbers of spheres [38]. While this system is superior in the rapid evaluation of tumor stem cells and/or their response to drug or radiation-related therapeutics, the spheres created through cell sorting currently do not include the surrounding cell types. Thus, as ACCs are highly innervated it remains to be seen whether these *ex vivo* settings, completely mimic the *in vivo* long-term response after treatment, which can be evaluated *via* the PDOX system.

At a minimum, primary tumors in our PDOX model provide greater in depth similarity with the patient's primary tumor, both biologically and molecularly. ACC11 PDOX(n) tumors recapitulated all 3 forms (cribriform, solid, tubular) characteristic for ACC's, while ACC PDX tissue altered their phenotype over multiple passages. Instead, PDOX tumors displayed similar pathological patterns amongst sibling and serial passages. This highlights the stability within and across multiple passages. Additionally, genomic and molecular alterations unique to the original ACC were retained. Based on these results, the PDOX salivary gland environment offers substantial benefits for tumor fidelity. Notably, the superiority of the PDOX model may be unique to ACCs, as a rare simultaneous comparison of PDX and PDOX with a pancreatic tumor showed that both maintained fidelity [39].

In contrast to the PDX-related transplantation of intact tumor fragments, the PDOX model includes cell-based injections. Remarkably, we still obtained all ACC epithelial (cribriform, solid and tubular form) and environmental characteristics with single cell transplantations, arguably better than with undissociated subcutaneous PDX tissue as it mimicked the original human ACC biopsy. As such, PDOX can be applied to newly generated ACC primary cell lines, such as from our PDX-derived ACC11 [14], or FACS-sorted ACC epithelial tumor stem cells that are currently evaluated for PDX formation capacity [38], to compare their fidelity in maintaining similar phenotypic characteristics of the original specimen. In the future, it will be essential to determine whether ACC cell lines, which are often enriched in a specific cell type, are able to generate mixed PDOX tumors. This could determine whether the glandular environment aids in forming mixed tumors, or whether the phenotype is inherently dictated by the tumor cells.

In summary, we describe an extensive validation of the newly established salivary gland PDOX model compared to the existing PDX model. The markedly poor outcome of patients developing ACCs highlights the need for more accurate models mimicking the clinical situation. Our glandular PDOX model presents a platform to better investigate the biology behind these aggressive salivary gland malignancies, and assess new drug strategies that can potentially be combined with current therapy of radiation.

Acknowledgements

We thank the histology (School of Dentistry) and sequencing core at the University of Michigan, MI.

Funding resources

This work was supported by the National Institutes of Health (NIH)/ National Institute of Dental and Craniofacial Research (NIDCR) grants DE022557, DE027034 (IML), and DE027551 (NJD).

Fig. 4. Evaluation of drug sensitivity and/or metastasis in the PDOX(n) and PDX-S model. (A) Tumor size of PDOX [4] tumors ($N = 3$) treated with Regorafineb or saline (control). Student's t-test, $^{*}P < .05$. (B, C) Bright field images and HE staining of lung tissue from control saline injected mouse and PDOX [3] mouse. Scale bar, 0.5 cm (B). Scale bar, 500 μm (upper panel) and 250 μm (lower panel). (C). Arrows indicate macrophage-like cells. (D) Macrophage marker CD68 and human-specific HNA staining on healthy human and mouse SMG (left), and healthy mouse and PDOX [3] lung tissue (middle and right). Scale bar, 50 μm (main 4 panels) and 25 μm (insets of lung). (E) Creation of the PDX-S model. (F) Examples of PDX-S tumors. Scale bar 0.5 cm. (G) Growth curve of PDX-S tumors ($N = 3$). (H) HE on PDX-S tissue. Scale bar, 500 μm (left) and 250 μm (right). (I, J) Protein staining on PDX-S tissue (I) and lung from the PDX-S mouse (J). Scale bar, 50 μm. qPCR of *MYB-NFIB* fusion in multiple samples, normalized to *GAPDH* and PDX. Human patient ACCX11 ($N = 1$), PDX (P8) ($N = 1$), PDOX [1] ($N = 1$), PDOX [3] ($N = 3$) and PDX-S ($N = 3$) tissue. Student's t-test with Welch's correction, $P < .1$. (L–M) qPCR analysis of various human specific genes in ACCX11 ($N = 1$), PDX (P8) ($N = 1$), PDOX [3] ($N = 3$), PDOX [1] ($N = 1$) and PDX-S ($N = 3$) tissue. Data was normalized to *GAPDH* and normal human SMG. Except for *Tubb3* and *Pecam*, data was normalized to mouse SMG and mouse *Gapdh*. Mean ± SEM. One sample t-test.

Declaration of interests

There is no conflict of interest.

Author contributions

IML and SA conceptualized the idea. IML wrote the paper, designed the studies, and managed the project. RLW provided control human biopsies. CAM provided the ACC11 PDX tissue and ACCX11 material. NJD analyzed and interpreted histology, co-designed some studies, and discussed experiments. AC, EH, HKA, GMIII and KY performed and analyzed experiments.

Appendix A. Supplementary data

Supplementary data to this article can be found online at https://doi.org/10.1016/j.ebiom.2019.02.011.

References

[1] Byrne AT, Alferez DG, Amant F, Annibali D, Arribas J, Biankin AV, et al. Interrogating open issues in cancer precision medicine with patient-derived xenografts. Nat Rev Cancer 2017;17(4):254–68.
[2] Dobrolecki LE, Airhart SD, Alferez DG, Aparicio S, Behbod F, Bentires-Alj M, et al. Patient-derived xenograft (PDX) models in basic and translational breast cancer research. Cancer Metastasis Rev 2016;35(4):547–73.
[3] Pompili L, Porru M, Caruso C, Biroccio A, Leonetti C. Patient-derived xenografts: a relevant preclinical model for drug development. J Exp Clin Cancer Res 2016;35(1):189.
[4] Hoffman RM. Patient-derived orthotopic xenografts: better mimic of metastasis than subcutaneous xenografts. Nat Rev Cancer 2015;15(8):451–2.
[5] Ben-David U, Ha G, Tseng YY, Greenwald NF, Oh C, Shih J, et al. Patient-derived xenografts undergo mouse-specific tumor evolution. Nat Genet 2017;49(11):1567–75.
[6] Blomme A, Van Simaeys G, Doumont G, Costanza B, Bellier J, Otaka Y, et al. Murine stroma adopts a human-like metabolic phenotype in the PDX model of colorectal cancer and liver metastases. Oncogene 2018;37(9):1237–50.
[7] Pearson AT, Finkel KA, Warner KA, Nor F, Tice D, Martins MD, et al. Patient-derived xenograft (PDX) tumors increase growth rate with time. Oncotarget 2016;7(7):7993–8005.
[8] Dillon PM, Chakraborty S, Moskaluk CA, Joshi PJ, Thomas CY. Adenoid cystic carcinoma: a review of recent advances, molecular targets, and clinical trials. Head Neck 2016;38(4):620–7.
[9] Moskaluk CA. Adenoid cystic carcinoma: clinical and molecular features. Head Neck Pathol 2013;7(1):17–22.
[10] Persson M, Andren Y, Mark J, Horlings HM, Persson F, Stenman G. Recurrent fusion of MYB and NFIB transcription factor genes in carcinomas of the breast and head and neck. Proc Natl Acad Sci U S A 2009;106(44):18740–4.
[11] Drier Y, Cotton MJ, Williamson KE, Gillespie SM, Ryan RJ, Kluk MJ, et al. An oncogenic MYB feedback loop drives alternate cell fates in adenoid cystic carcinoma. Nat Genet 2016;48(3):265–72.
[12] Wysocki PT, Izumchenko E, Meir J, Ha PK, Sidransky D, Brait M. Adenoid cystic carcinoma: emerging role of translocations and gene fusions. Oncotarget 2016;7(40):66239–54.
[13] Moskaluk CA, Baras AS, Mancuso SA, Fan H, Davidson RJ, Dirks DC, et al. Development and characterization of xenograft model systems for adenoid cystic carcinoma. Lab Invest 2011;91(10):1480–90.
[14] Chen C, Choudhury S, Wangsa D, Lescott CJ, Wilkins DJ, Sripadhan P, et al. A multiplex preclinical model for adenoid cystic carcinoma of the salivary gland identifies regorafenib as a potential therapeutic drug. Sci Rep 2017;7(1):11410.
[15] Panaccione A, Chang MT, Carbone BE, Guo Y, Moskaluk CA, Virk RK, et al. NOTCH1 and SOX10 are essential for proliferation and radiation resistance of cancer stem-like cells in adenoid cystic carcinoma. Clin Cancer Res 2016;22(8):2083–95.
[16] Fu XY, Besterman JM, Monosov A, Hoffman RM. Models of human metastatic colon cancer in nude mice orthotopically constructed by using histologically intact patient specimens. Proc Natl Acad Sci U S A 1991;88(20):9345–9.
[17] van Weert S, van der Waal I, Witte BI, Leemans CR, Bloemena E. Histopathological grading of adenoid cystic carcinoma of the head and neck: analysis of currently used grading systems and proposal for a simplified grading scheme. Oral Oncol 2015;51(1):71–6.
[18] Lombaert IM, Brunsting JF, Wierenga PK, Faber H, Stokman MA, Kok T, et al. Rescue of salivary gland function after stem cell transplantation in irradiated glands. PLoS One 2008;3(4):e2063.
[19] Lombaert IM, Abrams SR, Li L, Eswarakumar VP, Sethi AJ, Witt RL, et al. Combined KIT and FGFR2b signaling regulates epithelial progenitor expansion during organogenesis. Stem Cell Rep 2013;1(6):604–19.
[20] Li J, Perlaky L, Rao P, Weber RS, El-Naggar AK. Development and characterization of salivary adenoid cystic carcinoma cell line. Oral Oncol 2014;50(10):991–9.
[21] Cheuk W, Chan JK, Ngan RK. Dedifferentiation in adenoid cystic carcinoma of salivary gland: an uncommon complication associated with an accelerated clinical course. Am J Surg Pathol 1999;23(4):465–72.
[22] Ibrahimi OA, Eliseenkova AV, Plotnikov AN, Yu K, Ornitz DM, Mohammadi M. Structural basis for fibroblast growth factor receptor 2 activation in Apert syndrome. Proc Natl Acad Sci U S A 2001;98(13):7182–7.
[23] Rudd MF, Sellick GS, Webb EL, Catovsky D, Houlston RS. Variants in the ATM-BRCA2-CHEK2 axis predispose to chronic lymphocytic leukemia. Blood 2006;108(2):638–44.
[24] Furuse C, Sousa SO, Nunes FD, Magalhaes MH, Araujo VC. Myoepithelial cell markers in salivary gland neoplasms. Int J Surg Pathol 2005;13(1):57–65.
[25] Liebig C, Ayala G, Wilks JA, Berger DH, Albo D. Perineural invasion in cancer: a review of the literature. Cancer 2009;115(15):3379–91.
[26] Ju J, Li Y, Chai J, Ma C, Ni Q, Shen Z, et al. The role of perineural invasion on head and neck adenoid cystic carcinoma prognosis: a systematic review and meta-analysis. Oral Surg Oral Med Oral Pathol Oral Radiol 2016;122(6):691–701.
[27] Ko YH, Lee MA, Hong YS, Lee KS, Jung CK, Kim YS, et al. Prognostic factors affecting the clinical outcome of adenoid cystic carcinoma of the head and neck. Jpn J Clin Oncol 2007;37(11):805–11.
[28] DeRose YS, Wang G, Lin YC, Bernard PS, Buys SS, Ebbert MT, et al. Tumor grafts derived from women with breast cancer authentically reflect tumor pathology, growth, metastasis and disease outcomes. Nat Med 2011;17(11):1514–20.
[29] Fu X, Le P, Hoffman RM. A metastatic orthotopic-transplant nude-mouse model of human patient breast cancer. Anticancer Res 1993;13(4):901–4.
[30] Wang X, Fu X, Kubota T, Hoffman RM. A new patient-like metastatic model of human small-cell lung cancer constructed orthotopically with intact tissue via thoracotomy in nude mice. Anticancer Res 1992;12(5):1403–6.
[31] Fu X, Guadagni F, Hoffman RM. A metastatic nude-mouse model of human pancreatic cancer constructed orthotopically with histologically intact patient specimens. Proc Natl Acad Sci U S A 1992;89(12):5645–9.
[32] Sanden E, Dyberg C, Krona C, Gallo-Oller G, Olsen TK, Enriquez Perez J, et al. Establishment and characterization of an orthotopic patient-derived Group 3 medulloblastoma model for preclinical drug evaluation. Sci Rep 2017;7:46366.
[33] Furukawa T, Kubota T, Watanabe M, Kitajima M, Hoffman RM. Orthotopic transplantation of histologically intact clinical specimens of stomach cancer to nude mice: correlation of metastatic sites in mouse and individual patient donors. Int J Cancer 1993;53(4):608–12.
[34] Fu X, Hoffman RM. Human ovarian carcinoma metastatic models constructed in nude mice by orthotopic transplantation of histologically-intact patient specimens. Anticancer Res 1993;13(2):283–6.
[35] Hiroshima Y, Maawy A, Zhang Y, Zhang N, Murakami T, Chishima T, et al. Patient-derived mouse models of cancer need to be orthotopic in order to evaluate targeted anti-metastatic therapy. Oncotarget 2016;7(44):71696–702.
[36] Umeda M, Komatsubara H, Nishimatsu N, Oku N, Shibuya Y, Yokoo S, et al. Establishment and characterization of a human adenoid cystic carcinoma line of the salivary gland which is serially transplantable and spontaneously metastasises to the lung in nude mice. Oral Oncol 2002;38(1):30–4.
[37] Zanoni M, Piccinini F, Arienti C, Zamagni A, Santi S, Polico R, et al. 3D tumor spheroid models for in vitro therapeutic screening: a systematic approach to enhance the biological relevance of data obtained. Sci Rep 2016;6:19103.
[38] Keysar SB, Eagles JR, Miller B, Jackson BC, Chowdhury FN, Reisinger J, et al. Salivary gland cancer patient-derived xenografts enable characterization of cancer stem cells and new gene events associated with tumor progression. Clin Cancer Res 2018;24(12):2935–43.
[39] Jun E, Hong SM, Yoo HJ, Kim MB, Won JS, An S, et al. Genetic and metabolic comparison of orthotopic and heterotopic patient-derived pancreatic-cancer xenografts to the original patient tumors. Oncotarget 2018;9(8):7867–81.